Magnetism and ultrafast magnetization dynamics of Co and CoMn alloys at finite temperature

R. Chimata,[1,*] E. K. Delczeg-Czirjak,[1] A. Szilva,[1] R. Cardias,[1,2] Y. O. Kvashnin,[1] M. Pereiro,[1] S. Mankovsky,[3] H. Ebert,[3] D. Thonig,[1] B. Sanyal,[1] A. B. Klautau,[2] and O. Eriksson[1]

[1]*Department of Physics and Astronomy, Material Theory, University Uppsala, SE-75120 Uppsala, Sweden*

[2]*Faculdade de Física, Universidade Federal do Pará, Belém, PA, Brazil*

[3]*Department of Chemistry, University of Munich, Butenandtstrasse 5-13, D-81377 Munich, Germany*

(Received 27 September 2016; revised manuscript received 22 April 2017; published 22 June 2017)

Temperature-dependent magnetic experiments such as pump-probe measurements generated by a pulsed laser have become a crucial technique for switching the magnetization in the picosecond time scale. Apart from having practical implications on the magnetic storage technology, the research field of ultrafast magnetization poses also fundamental physical questions. To correctly describe the time evolution of the atomic magnetic moments under the influence of a temperature-dependent laser pulse, it remains crucial to know if the magnetic material under investigation has magnetic excitation spectrum that is more or less dependent on the magnetic configuration, e.g., as reflected by the temperature dependence of the exchange interactions. In this paper, we demonstrate from first-principles theory that the magnetic excitation spectra in Co in fcc, bcc, and hcp structures are nearly identical in a wide range of noncollinear magnetic configurations. This is a curious result of a balance between the size of the magnetic moments and the strength of the Heisenberg exchange interactions, that in themselves vary with configuration, but put together in an effective spin Hamiltonian results in a configuration-independent effective model. We have used such a Hamiltonian, together with *ab initio* calculated damping parameters, to investigate the magnon dispersion relationship as well as ultrafast magnetization dynamics of Co and Co-rich CoMn alloys.

DOI: 10.1103/PhysRevB.95.214417

I. INTRODUCTION

Ultrafast magnetism, with relevant time scales being an order of a few picoseconds, has become an intense research field. The motivation may be found both in fundamental aspects as well as practical implications of these phenomena. Most of the information stored technologically is done in a magnetic medium. Hence, the possibility to write and retrieve information in a magnetic material at a high speed and with low-energy consumption has obvious societal implications. For this reason, ultrafast magnetization dynamics has naturally become an intense research field. The experiment by Beaurepaire and co-workers [1] represents a breakthrough experiment, with several experimental studies that followed [2–8]. However, despite several years of intense investigations, a microscopic understanding of the processes of ultrafast magnetization dynamics is far from being established.

The most common experimental technique is by pump probe, where an optical laser pulse excites the electron subsystem. The excited electrons become thermalized quickly [9] and the thermal energy of the electron subsystem is transferred to the spin and lattice subsystems. This defines three thermal reservoirs and typically the three reservoirs reach thermal equilibrium after some 10–20 ps. The time evolution of the temperatures of these reservoirs may be quantified by the so-called three-temperature model [1,10,11]. It should be noted that in the first few picoseconds of a pump-probe experiment, the material is not in thermal equilibrium between the three reservoirs, but at a sufficiently long time after the pump pulse, the temperature is the same in different subsystems.

On the theoretical side, it has been argued that atomistic spin-dynamics simulations should be relevant over a time scale of picoseconds and longer [12]. The argument here is that a description of atomistic moments is relevant, and that these moments evolve in time with a spin temperature that is given by the three-temperature model [13]. In this description, the magnetic moments and all parameters of an effective spin Hamiltonian are evaluated from first-principles theory. Coupled to the equations of motion of the atomic spins [14], this allows for numerical results of the time evolution of the magnetic moments, forming an *ab initio* theory that does not rely on experimental results as input. The dominating parameters of such a spin Hamiltonian are the size of the atomic moments coupled to the interatomic exchange interaction [15]. To mention an example of the fruitfulness of this approach, we note that the first experimental result of fcc Ni was reproduced by such simulations with good accuracy [16].

Recently, it was shown that the interatomic exchange interactions of bcc Fe have a distinct temperature dependence, and only a good agreement with experimental room-temperature magnon excitations was achieved when the exchange parameters were evaluated at room temperature [17]. This demonstrates that if a too broad temperature interval needs to be covered, bcc Fe is not an ideal Heisenberg system, and that the normal concepts of a Heisenberg Hamiltonian, e.g., magnons, can still be considered although configuration-dependent exchange parameters must be evaluated and used. This puts high demands if a three-temperature model is attempted to be used to reproduce an experimental pump-probe experiment since at each time step the exchange parameters (and magnetic moment) should in principle be recalculated, in order to take the changing temperature of the spin system into account. If a material is a good Heisenberg system or not, i.e., if the exchange parameters are independent on the temperature or not, is difficult to stipulate before a first-principles calculation of the configurational-dependent exchange parameters has

*raghuveer.chimata@physics.uu.se

been made, but several systems have by now been suggested to have exchange parameters that depend more or less strongly on temperature. Hence, it seems that there are indeed very few materials that are good Heisenberg systems. In this paper, we demonstrate that Co, in fcc, bcc, and hcp structures, is rather unique in this sense, at least among the elemental metals, displaying the features of a Heisenberg magnet in a wide range of magnetic configurations. As we shall see below, this comes with a twist since both the values of the magnetic moments and the strength of the Heisenberg exchange parameters depend on configuration, but put together in a spin Hamiltonian, they form a model that curiously is configuration independent. We also investigate the magnetization dynamics of this system, and compare it to a Co-Mn alloy in the bcc and bct structures.

The paper is organized as follows. In Sec. II, we present the theoretical tools used to describe the ground state and dynamical properties. Section III contains the numerical details of the calculations. Results and discussions are presented in Sec. IV. Finally, we give conclusions in Sec. V.

II. METHODS

In order to investigate ultrafast demagnetization dynamics of Co and Co-Mn alloys, we combined first-principles electronic structure calculations with atomistic spin-dynamics simulations. These methods are described below.

A. Electronic structure calculations

The ground-state electronic structure and magnetic properties of the studied materials are obtained via density functional theory (DFT) calculations. The Kohn-Sham equations are solved within the Korringa-Kohn-Rostoker (KKR) Green's function formalism as implemented in the spin-polarized relativistic KKR (SPR-KKR) package [18], and within linear muffin-tin orbital method [19] in atomic sphere approximation (LMTO-ASA). We used both real-space (RS) [20] and reciprocal-space [21] realizations of LMTO-ASA. The relativistic effects are considered by solving the fully relativistic Dirac equation [22]. Substitutional disorder is treated by making use of the coherent potential approximation (CPA) [23]. The high-temperature paramagnetic phase was modeled by disordered local moment (DLM) approximation [24,25] in combination with CPA. Here, the Co-Mn binary systems were treated as quaternary $(\mathrm{Co}^{\uparrow}_{0.5}\mathrm{Co}^{\downarrow}_{0.5})_{1-x}(\mathrm{Mn}^{\uparrow}_{0.5}\mathrm{Mn}^{\downarrow}_{0.5})_{x}$ alloys, with a random mixture of the two magnetic orientations of Co and Mn. DLM approach is believed to accurately describe the high-temperature paramagnetic phase [24], therefore, we apply this tool, in case of alloys, to evaluate whether the local magnetic moments and magnetic coupling constants are sensitive to the temperature-induced fluctuations or not.

The interatomic exchange interactions J_{ij} are calculated via the Liechtenstein-Katsnelson-Antropov-Gubanov formalism (LKAG) [15] as implemented in the SPR-KKR and the RS-LMTO-ASA codes and its extension to noncollinear spin arrangement [17] (see Sec. II B). The site- and element-resolved Gilbert damping parameters (α, α_1(Co), α_2(Mn)) are calculated based on the linear response formalism [26] (see Sec. II C).

B. Calculation of the interatomic J_{ij} exchange parameters

Interatomic magnetic exchange interaction parameters J_{ij} are calculated from first principles. For collinear atomic spin alignment, the method of infinitesimal spin rotation was derived almost 30 years ago [15]. The energy (grand potential) variation can be calculated when the atomic spin is rotated by a small angle simultaneously, and mapped onto a bilinear spin model:

$$\mathcal{H} = -\frac{1}{2}\sum_{i\neq j} J_{ij}\vec{e}_i \cdot \vec{e}_j, \tag{1}$$

where the unit vector $\vec{e}_i$ ($\vec{e}_j$) denotes the direction of the spin at site i (j). Although it might seem trivial, we write also this spin Hamiltonian in the more common form, that explicitly describes the coupling of atomic spin moments, $\vec{m}$:

$$\mathcal{H} = -\frac{1}{2}\sum_{i\neq j} \tilde{J}_{ij}\vec{m}_i \cdot \vec{m}_j. \tag{2}$$

For the discussion of our results (below) it becomes relevant to make a distinction between Eqs. (1) and (2), and the fact that J_{ij} and $\tilde{J}_{ij}$ differ only by a factor $m_i m_j$, where $\vec{m}_i = m_i\vec{e}_i$.

The LKAG interatomic exchange formula can be written as $J_{ij} = A_{ij}^{\uparrow\downarrow}$, where the symbols $\uparrow$ and $\downarrow$ refer to the up- and down-spin channels, respectively, while

$$A_{ij}^{\alpha\beta} = \frac{1}{\pi}\int_{-\infty}^{E_F} d\varepsilon\, \mathrm{Im}\,\mathrm{Tr}_L\left(p_i T_{ij}^{\alpha} p_j T_{ji}^{\beta}\right). \tag{3}$$

For collinear spin configuration, the corresponding $T_{ij}^{\uparrow}$ and $T_{ij}^{\downarrow}$ matrices denote the component of the scattering path operator (SPO), τ_{ij}, in the two spin channels between sites i and j while p_i and p_j stand for the (spin part) of the inverse of the one-site scattering matrix [15]. In order to treat alloys or alloy analogy models, the defect atom μ is created at site i by a defect matrix D_i^{μ}. This defect matrix is considered in the effective CPA medium $\tilde{\tau}_{i\mu,j\nu} = D_i^{\mu}\tau_{ij}^{\mathrm{CPA}}D_j^{\nu}$ [27]. Hence, the scattering path operator $\tilde{\tau}_{i\mu,j\nu}$ replaces related components of the scattering path operator in Eq. (3).

In a noncollinear spin arrangement, the SPO matrix elements can be grouped into a charge and spin part with the help of the 2×2 unit matrix and the Pauli matrices. Hence, one can define the exchange matrix $A_{ij}^{\alpha\beta}$ where indices α and β run over 0, x, y, or z. By using trace properties, the general symmetry relation $A_{ij}^{\alpha\beta} = A_{ji}^{\beta\alpha}$ was found. In the absence of spin-orbit coupling, we can write that $(T_{ij}^{\alpha})^T = T_{ji}^{\alpha}$, which implies that $A_{ij}^{\alpha\beta} = A_{ij}^{\beta\alpha}$, i.e., the A matrix is symmetric. The grand potential (pairwise) variation is proportional to the variation of the integrated density of states, which is determined by the Lloyd formula [28]. This leads to the expression

$$\delta E_{ij} = -2J_{ij}^{nc}\delta\vec{e}_i\delta\vec{e}_j - 4\sum_{\alpha,\beta=x,y,z}\delta e_i^{\alpha}A_{ij}^{\alpha\beta}\delta e_j^{\beta} \tag{4}$$

when the spin-orbit interaction is not considered, where

$$J_{ij}^{nc} = A_{ij}^{00} - A_{ij}^{xx} - A_{ij}^{yy} - A_{ij}^{zz}. \tag{5}$$

At low temperatures, where the degree of noncollinearity between atomic spins is small (a regime we denote the

quasicollinear regime), the second term of Eq. (4) does not give a significant contribution, hence, we will here resolve J_{ij}^{nc} for different systems, which can be mapped onto Eq. (1), i.e., onto a Heisenberg model when the calculated exchange parameters are spin configuration independent. Note that in the exact collinear limit (e.g., in ferromagnetic ground state), Eq. (5) reduces to the expression $A_{ij}^{00} - A_{ij}^{zz}$, and it can be shown that this is equal to the LKAG formula given by $A_{ij}^{\uparrow\downarrow}$.

C. Element- and site-resolved damping parameters

Within this work, the Gilbert damping parameter is calculated on the basis of the linear response formalism [26]. The approach used derives from a representation of the electronic structure in terms of the Green function $G^{+}(E)$ that in turn is determined by means of the multiple scattering formalism [18]. The diagonal elements $\mu = x,y,z$ of the Gilbert damping tensor can be written as [26]

$$\alpha^{\mu\mu} = \frac{g}{\pi m_{\mathrm{tot}}} \sum_{j} \mathrm{Tr}\langle \underline{\mathcal{T}}_0^{\mu}\, \underline{\tilde{\tau}}_{0j}\, \underline{\mathcal{T}}_j^{\mu}\, \underline{\tilde{\tau}}_{j0}\rangle_c, \tag{6}$$

where the effective g factor $g = 2(1 + m_{\mathrm{orb}}/m_{\mathrm{spin}})$ and total magnetic moment $m_{\mathrm{tot}} = m_{\mathrm{spin}} + m_{\mathrm{orb}}$ are given by the spin and orbital moments m_{spin} and m_{orb}, respectively, ascribed to a unit cell. Equation (6) gives $\alpha^{\mu\mu}$ for the atomic cell at lattice site 0 and implies a summation over contributions from all sites indexed by j including $j = 0$. The elements of the matrix $\underline{\tilde{\tau}}_{0j}$ are given by $\tilde{\tau}_{0j}^{\Lambda\Lambda'} = \frac{1}{2i}(\tau_{0j}^{\Lambda\Lambda'} - \tau_{0j}^{\Lambda'\Lambda})$ where $\underline{\tau}_{0j}$ is the so-called SPO matrix [26] evaluated for the Fermi energy E_F. Finally, the matrix $\underline{\mathcal{T}}_j^{\mu}$ is represented by the matrix elements

$$\mathcal{T}_j^{\mu,\Lambda'\Lambda} = \int d^3r \left[Z_j^{\Lambda'}(\vec{r})\right]^{\times} [\beta\sigma^{\mu} B_{xc}(\vec{r})] Z_j^{\Lambda}(\vec{r}) \tag{7}$$

of the torque operator $\hat{\mathcal{T}}^{\mu} = \beta(\vec{\sigma} \times \hat{m}_z)_{\mu} B_{xc}(\vec{r})$ [29]. Here, $Z_j^{\Lambda}(\vec{r})$ is a regular solution to the single-site Dirac equation for the Fermi energy E_F labeled by the combined quantum numbers $\Lambda = (\kappa,\mu)$, with κ and μ being the spin-orbit and magnetic quantum numbers [30].

To calculate the configurational average indicated by the brackets $\langle \ldots \rangle_c$, in the case of disordered alloys, the CPA alloy theory is used. This is done using the scheme developed by Butler [31] in the context of electrical conductivity, that splits the summation in Eq. (6) into a site diagonal part $\langle \underline{\mathcal{T}}_0 \mu\, \underline{\tilde{\tau}}_{00}\, \underline{\mathcal{T}}_0^{\mu}\, \underline{\tilde{\tau}}_{00}\rangle_c$, and a site off-diagonal part $\sum_{j\neq 0} \langle \underline{\mathcal{T}}_0^{\mu}\, \underline{\tilde{\tau}}_{0j}\, \underline{\mathcal{T}}_j^{\mu}\, \underline{\tilde{\tau}}_{j0}\rangle_c$, respectively. Dealing with the second term, one has to account in particular for the so-called "in-scattering processes" that deals with vertex corrections of crucial importance for the Gilbert damping [32].

As indicated above, Eq. (6) gives in the case of a unit cell involving in the case of an alloy several atomic types a value for $\alpha^{\mu\mu}$ that is averaged over these types. In the case of a system consisting only of magnetic components, i.e., none of its components have an induced magnetic moment, one may also introduce a type-projected damping parameter $\alpha_t^{\mu\mu}$. As the average for the site diagonal as well as site off-diagonal contributions to $\alpha^{\mu\mu}$ involve a sum over the types t with the type-specific contribution weighted by the corresponding concentration x_t [31], one is led in a natural way to the expression

$$\alpha_t^{\mu\mu} = \frac{g_t}{\pi m^t} \mathrm{Tr}\, \underline{\mathcal{T}}_0^{\mu} \Bigg[\langle \underline{\tau}_{00} \underline{\mathcal{T}}_0^{\mu} \underline{\tau}_{00} \rangle_{t\ on\ 0} + \sum_{j\neq 0} \sum_{t'\ on\ j} x_{t'} \langle \underline{\tilde{\tau}}_{0j} \underline{\mathcal{T}}_j^{\mu} \underline{\tilde{\tau}}_{j0} \rangle_{t\ on\ 0;\, t'\ on\ j} \Bigg] \tag{8}$$

with t and t' denoting the atomic types at the lattice positions 0 and j, respectively. Here, we use a type-specific g factor g_t and magnetic moment m^t given by the corresponding spin and orbital moments m_{spin}^t and m_{orb}^t, respectively. The resulting definition for the element-projected Gilbert damping $\alpha_t^{\mu\mu}$ leads now to an average for the unit cell according to $\alpha^{\mu\mu} = \sum_t x_t \alpha_t^{\mu\mu}$. Because of the normalizing factor g/m_{tot} used in Eq. (6), this expression will lead in general to results slightly deviating from that based on Eq. (6).

The calculations of the Gilbert damping parameter for finite temperature presented below have been done using the so-called alloy analogy model [26]. This approach is based on the adiabatic approximation assuming random temperature-dependent displacements of the atoms from their equilibrium positions. Using a discrete set of displacements with each displacement treated as an alloy component, the problem of calculating the thermal average for a given temperature T is reduced to the problem of calculating the configurational average as done for substitutional alloys [26].

D. Atomistic spin dynamics

The temperature-dependent evolution of spins is calculated from atomistic spin-dynamics (ASD) simulation at different temperatures using the framework of Landau-Lifshitz-Gilbert (LLG) formalism. The temporal evolution of an atomic moment in LLG formalism is given by [14]

$$\frac{d\vec{m}_i(t)}{dt} = -\frac{\gamma}{(1+\alpha^2)} \left(\vec{m}_i(t) \times \vec{B}_i(t) + \frac{\alpha}{m_i} \vec{m}_i(t) \times [\vec{m}_i(t) \times \vec{B}_i(t)] \right), \tag{9}$$

where γ is the gyromagnetic ratio, α represents the dimensionless Gilbert damping constant, and $\vec{m}_i$ stands for an individual atomic moment on site i. Note that $\vec{m}_i = m_i \vec{e}_i$ where m_i is the magnitude of the magnetic moment (at site i). The effective magnetic field is represented by $\vec{B}_i = -\frac{\partial \mathcal{H}}{\partial \vec{m}_i} + \vec{b}_i$, where $\mathcal{H}$ is given by Eq. (2) and $\vec{b}_i$ is a time-evolved stochastic magnetic field, which depends on the spin temperature evaluated from the two-temperature (2T) model [33].

The analytical expression of the two-temperature model reads as

$$T_s = T_0 + (T_P - T_0) \times (1 - \exp^{(-t/\tau_{\mathrm{initial}})}) \times \exp^{(-t/\tau_{\mathrm{final}})} + (T_F - T_0) \times (1 - \exp^{(-t/\tau_{\mathrm{final}})}), \tag{10}$$

where T_s is the spin temperature, T_0 is the initial temperature of the system, T_P is the peak temperature after the laser pulse is applied, and T_F is the final temperature. τ_{initial} and τ_{final} are exponential parameters. The calculated spin temperature from Eq. (10) is explicitly passed into LLG equation via the

TABLE I. Theoretically estimated lattice parameters (a), total (M) and element (m_{Co}, m_{Mn}) projected magnetic moments, Curie temperatures (T_C), total and element projected densities of states at the Fermi level [DOS(E_F)], and Gilbert damping parameters (α) calculated for bcc, fcc, and hcp Co as well as for $Co_{1-x}Mn_x$ ($x = 0.1,0.15,0.2,0.3$) alloys in the bcc and bct crystallographic phases. The experimental Curie temperatures, lattice constants, magnetic moments are shown in brackets and the DLM results are shown in parentheses. The magnetic moments are calculated using experimental lattice parameters.

System	a/c (Å)	M (μ_B/atom)	T_C (K)	DOS(E_F) (states/Ry)	α
bcc Co	2.85[2.83] [45]	1.70[1.77, 1.50] [45,46]	1280	25.3(31.448)	0.0091(0.011)
fcc Co	3.58[3.54] [47]	1.62[1.68] [50]	1311[1392] [61]	16.8(29.170)	0.0057(0.009)
hcp Co	2.48/4.04[2.50/4.05] [62]	1.59[1.52] [51]	1306[1388] [60]	12.8(28.68)	0.0030(0.019)

System		M	m_{Co}	m_{Mn}		Total	Co	Mn	α	α_1(Co)	α_2(Mn)
$Co_{0.90}Mn_{0.10}$ [63]	2.86	1.89	1.77(1.51)	2.99(2.75)	1280(1054)	20.1	21.6	7.1	0.0072	0.0083	0.0013
$Co_{0.85}Mn_{0.15}$ [63]	2.87	1.96	1.78	2.98	1248	19.5	21.2	9.1	0.0066	0.0081	0.0015
$Co_{0.80}Mn_{0.20}$	2.88	2.03	1.79	2.97	1129	18.3	20.2	11.0	0.0058	0.0076	0.0016
$Co_{0.70}Mn_{0.30}$	2.89	2.13	1.80(1.46)	2.89(2.72)	1050(833)	16.0	17.5	12.7	0.0045	0.0061	0.0022
$Co_{0.90}Mn_{0.10}$ bct	2.83 [2.71] [43]	1.79	1.69	2.73	1235[1215] [43]	19.1	20.2	9.0	0.0080	0.0090	0.0025
$Co_{0.70}Mn_{0.30}$ bct	2.87 [2.90] [43]	2.11	1.80	2.85	1054 [842] [43]	16.8	17.6	14.9	0.0047	0.0062	0.0025

stochastic magnetic field $\vec{b}_i$ in Eq. (9), which takes into account thermal fluctuations of the system and the strength of the stochastic field is defined as $D = \frac{\alpha k_B T_s}{\gamma m}$, k_B is the Boltzmann constant. Alloying Co is treated by spatial random disorder of the Mn dopant.

The dynamical structure factor, which describes the magnon dispersion relation, is obtained from the Fourier transform of space and time displaced correlation function

$$C^{\mu}(\vec{r},\vec{r}',t) = \left\langle m^{\mu}_{\vec{r}}(t) m^{\mu}_{\vec{r}'}(0)\right\rangle - \left\langle m^{\mu}_{\vec{r}}(t)\right\rangle \left\langle m^{\mu}_{\vec{r}'}(0)\right\rangle, \tag{11}$$

where the ensemble average is represented in the angular brackets and $\mu = x,y,z$ is the Cartesian component, and its Fourier transform is written as

$$S^{\mu}(\vec{q},\omega) = \frac{1}{\sqrt{2\pi}N} \sum_{\vec{r},\vec{r}'} e^{i\vec{q}\cdot(\vec{r}-\vec{r}')} \int_{-\infty}^{\infty} dt\ e^{i\omega t} C^{\mu}(\vec{r},\vec{r}',t), \tag{12}$$

where $\vec{q}$ and ω are the momentum and energy transfer, respectively. N is the number of terms in the summation.

To estimate the Curie temperatures, we used the fourth-order size-dependent Binder cumulant [34], which is defined as

$$U_L = 1 - \frac{\langle M^4\rangle_L}{3\langle M^2\rangle_L^2}, \tag{13}$$

where M is the total or average magnetization. $\langle \ldots \rangle$ is the ensemble and time average. Binder cumulants exploit the critical point and critical exponents in a phase transition from the crossing point of magnetization curves for different sizes L of the system.

III. NUMERICAL DETAILS

The Perdew, Burke, and Ernzerhof (PBE) [35] version of the generalized gradient approximation is used to describe the exchange-correlation potential. The spin-polarized scalar relativistic full-potential (SR-FP) mode [18] is used to calculate the total energies as a function of volume [$E(V)$] and the total (M) and element-resolved (m_{Co}, m_{Mn}) magnetic moments. For the exchange integral (J_{ij}) and damping parameter (α, α_1(Co), α_2(Mn)) calculations, the potential is described within the atomic sphere approximation (ASA) using the scalar-relativistic (SR) and relativistic (R) modes, respectively [18,32]. The basis set consisted of s, p, d, and f orbitals ($l_{max} = 3$). The number of $\vec{k}$ points was set to ≈300, ≈500, and ≈1 000 000 for the calculation of the ground-state properties, density of states (magnetic exchange integrals), and site- and element-resolved damping parameters, respectively. Equilibrium lattice constants are obtained by fitting $E(V)$ curves with a Morse type of equation of state [36]. The exchange constants are calculated up to 12 nearest-neighbor shells.

We performed ASD simulations by using the UPPASD software [12,37] for the Co-based systems with a size of 20 × 20 × 20 unit cells employing periodic boundary conditions. Here, we used calculated exchange constants from *ab initio* and 16 ensembles were considered for averaging.

IV. RESULTS AND DISCUSSION

A. Static properties of Co and Co-Mn alloys

1. *Electronic structure and magnetic properties*

The estimated theoretical lattice parameters (a) are listed in Table I for bcc, fcc, and hcp Co as well as $Co_{1-x}Mn_x$ alloys in the bcc and bct crystallographic phases, calculated using the PBE exchange-correlation functional. The local density approximation (LDA) calculations underestimate the lattice parameter by about 2% when compared to PBE. The presented PBE values for pure Co are in good agreement with the experimental data found for bcc Co grown in GaAs surface (2.82 Å) [38] and for fcc Co/Cu film (3.54 Å) [39], as well as with the results of the previous DFT simulations [40]. The Co-Mn alloys can be grown on a GaAs surface in bcc [41,42] or bct [43,44] crystal structure. The theoretical lattice constant a of bcc alloys increases with Mn addition, which is consistent with the larger atomic radius for Mn compared to Co. The estimated lattice constants for $x = 0.3$ (see Table I) and $x = 0.4$ (2.89 Å) is in line with the experimental lattice parameters data reported for $x = 0.32$ (0.4) [41,42] which is 2.9 (2.89) Å. The in-plane lattice parameter for the bct phase of $Co_{0.90}Mn_{0.10}$ and $Co_{0.70}Mn_{0.30}$ alloys is taken from

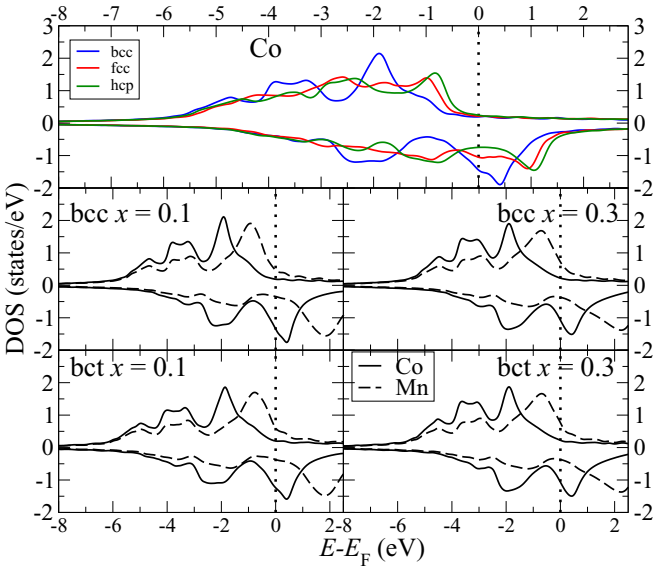

FIG. 1. Density of states (DOS) per atom of bcc Co (blue), fcc Co (red), hcp Co (green) (upper panel), and bcc and bct $Co_{1-x}Mn_x$ (lower panel). DOS for Co in $Co_{1-x}Mn_x$ alloys is labeled by full line while DOS of Mn is represented by dashed line. Dotted line illustrates the Fermi energy.

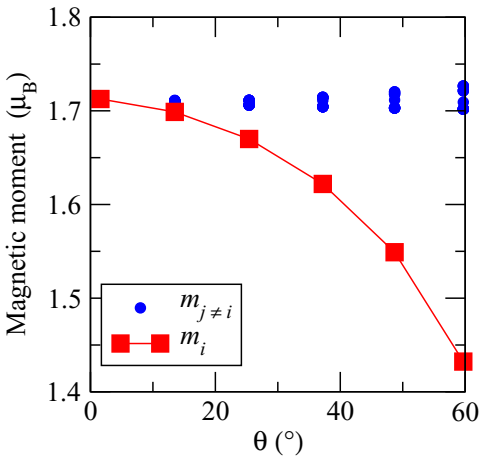

FIG. 2. Calculated magnetic moment as a function of rotation of a single spin with an angle θ, in the FM background of bcc Co.

experiments, Refs. [43,44], respectively, while the out-of-plane lattice parameters have been optimized theoretically (see Table I).

Calculated densities of states (DOS) for pure Co in bcc, fcc, and hcp crystal structure are presented in Fig. 1. For these crystal structures, the 3*d* majority spin channel is fully occupied, resulting in a low DOS at the Fermi level $DOS^{\uparrow}(E_F)$, while $DOS^{\downarrow}(E_F)$ lies near a peak in the 3*d* DOS. The energy split between the majority and minority channels leads to a magnetic moment of 1.73 μ_B for the bcc lattice, in good agreement with the previous theoretical data [40,46]. The experimental value for the magnetic moments of Co in the bcc structure is estimated from Co films grown on GaAs [45,48]. The average value is given as 1.4 μ_B but in the center of the film (50 Å) the estimated experimental value for the Co magnetic moment in the bcc structure is ~1.7 μ_B [48] which is in good agreement with the theoretically estimated value. For fcc Co, the calculated magnetic moment is in agreement with the previously published theoretical value of 1.64 μ_B [40,49] and in decent agreement with the experimental value of 1.68 μ_B [50]. Finally, the magnetic moment of hcp Co is in good agreement with the reported experimental [51] and theoretical data [40].

In both bcc and bct phases of Co-Mn alloys, the $DOS^{\uparrow}(E_F)$ of Co is small due to the full occupation of the 3*d* majority channels, and the shift in the occupation of the majority and minority channels results in a magnetic moment higher than that in pure bcc Co and it is found to increase with increased Mn content (see Table I). The Mn 3*d* majority band is not fully occupied, and the 3*d* minority band contains less states than in case of Co, due to the reduced number of electrons for Mn. The exchange splitting results in a higher magnetic moment for Mn than for Co (see Table I). As Table I shows for Co-Mn alloys, the coupling between Co and Mn moments is ferromagnetic, with a large moment on both atoms. The results for the bcc structure give larger moments compared to data for the bct structure.

The smallest magnetic moments are given by the SR-FP mode. The SR-ASA (R spin) moments are in average 0.6% (0.5%) larger compared to the SR-FP moments. We find the same trends for SR-ASA and R spin moments as a function of composition and structure as in the case of SR-FP moments. The orbital moment of Co is 0.085 μ_B in the bcc phase. Its variation among different crystal structures and alloying is within 7% and follows the same trend as for the spin moments. The orbital moment of Mn in bcc $Co_{0.9}Mn_{0.1}$ is 0.018 μ_B. This value decreases to 0.016 μ_B for $x = 0.3$ Mn content in the bcc phase. The orbital moment of Mn in the bct phase is smaller compared to its value in the bcc phase for the corresponding composition. Local magnetic moments of Co and Mn in the DLM phase of $Co_{1-x}Mn_x$ for $x = 0.1$ and 0.3 are also presented in Table I. Here, we find that m_{Co} and m_{Mn} are reduced with 15% and 20%, respectively, in the DLM phase compared to that of FM solution.

All entries in Table I show that the DLM configuration results in lower magnetic moments than for the FM configuration. To analyze this further, we calculated the size of the magnetic moment of a supercell of 16 atoms in a bcc lattice, in which only the central atom had its magnetic moment rotated away from the z axis with an angle θ. The rotated moment is denoted as m_i and the rest of the spins are labeled m_j. The self-consistently obtained values of m_i and m_j are shown for each value of θ in Fig. 2. One can see that once θ increases, the magnitude of the moment m_i tends to decrease. We repeated the same calculations for bcc Fe and obtained qualitatively the same behavior. Thus, the results of Fig. 2 are consistent with the data in Table I, and seem to reflect a quite general phenomenon that the rotation of a moment in a system with predominant FM interactions leads to the decrease of its length. This fact can be understood on the basis of a simple model, containing the energy of longitudinal spin variation (containing even powers of magnetization, as appropriate for a Landau expansion) and a nearest-neighbour exchange coupling (J_1). In the case of the single-spin rotation

in the ferromagnetic background, one obtains

$$E = -\alpha_1 m_i^2 - \alpha_2 M^2 + \beta_1 m_i^4 + \beta_2 M^4 - \tilde{J}_1 \vec{m}_i \cdot \vec{M}, \quad (14)$$

where $M = \sum_{j=1}^{N} m_j$ represents the macrospin formed by all N nearest-neighbor spins from the FM background. The parameters α_1, α_2, β_1, and β_2 are phenomenological constants originating from the local exchange interactions. The energy penalty stemming from the Heisenberg term when rotating the moment m_i with an angle θ will be given by

$$E(\theta) - E(0) = \tilde{J}_1 m_i M[1 - \cos(\theta)]. \quad (15)$$

It is straightforward to show that, if the magnitude of m_i is allowed to change, the system will try to minimize the energy costs of the single-spin rotation by decreasing its length. In principle, a reduction of M would also reduce the energy cost of rotating a single spin, but the Landau parameters describing this change are not in favor of this scenario. Finding the minima of the energy with respect to m_i leads to the solution of nonlinear equation, which can be solved numerically. The numerical results confirm that with an increase of θ, the value of m_i corresponding to the minimum of the energy goes down.

Thus, for the case of a single-spin rotation in bcc Co, we have shown that the magnitude of the magnetic moments unavoidably depends on the magnetic configuration. In order to quantify how sensitive the magnetic excitations to interatomic noncollinearity, we have performed a series of spin spiral calculations [52] for the same structure. Spin spiral states are characterized by the propagation direction ($\vec{q}$) and the cone angle Ω between the magnetization and $\vec{q}$ vectors. Note that spin spirals with infinitesimal Ω would correspond to the actual magnon excitation. The bottom panel of Fig. 3 shows the self-consistently obtained value of the magnetic moment in all different spin spiral states. Just as in the case of the single-spin rotation (Fig. 2), the magnetic moment experiences a variation when $\vec{q}$ is changed. In the top panel of Fig. 3 we show the relative energies of the spin spirals calculated for various $\vec{q}$ and Ω values. On the y axis we plot $E_{\vec{q}} - E_{q=0}/\sin^2(\Omega)$, which is supposed to be Ω independent for a truly Heisenberg magnet (see, e.g., Ref. [53]). It is clearly seen from Fig. 3 that, despite the changes in the magnetic moment values, all curves lie nearly on top of each other, if Ω lies within the range of 5° to 45°. At larger Ω angles, most of spin spiral energies are still very close to each other and the largest differences appear for $\vec{q}$ vectors along Γ-H direction. Hence, one can see that Co is a remarkable system, which is characterized by a configuration-independent magnetic excitation in a wide range of magnetic states. From Fig. 3 we estimated that the Heisenberg Hamiltonian [Eq. (1)] is perfectly valid up to a critical value of the angle between the nearest-neighboring spins of about 90°. Quite importantly, the results indicate an intriguing interplay between the strength of the $\tilde{J}_{ij}$'s and the magnitude of $\vec{m}_i$'s, which tends to balance each other resulting in configuration independent J_{ij}'s.

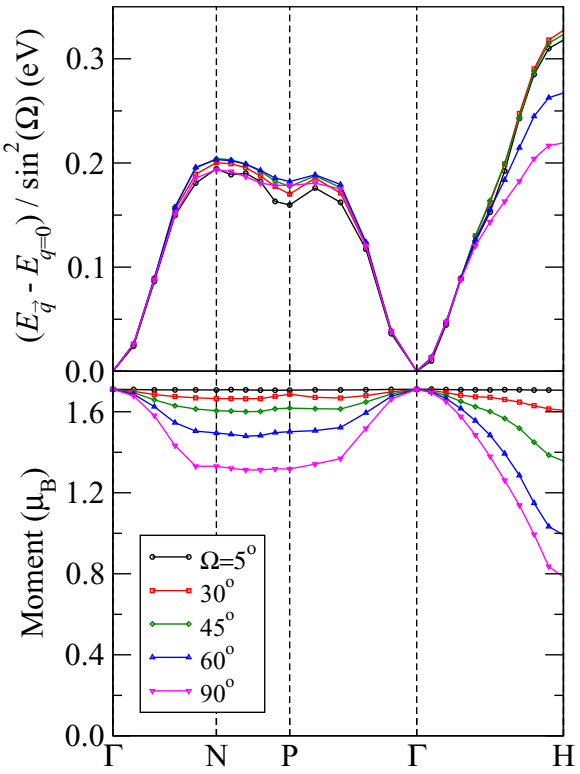

FIG. 3. Calculated relative spin spiral energies for different values of cone angle Ω along with the self-consistent values of the magnetic moment as a function of the propagation vector $\vec{q}$.

2. *Temperature-dependent exchange interactions* J_{ij}

The calculated exchange interactions J_{ij} for all Co-based systems at $T = 0\,\mathrm{K}$ are plotted in Fig. 4. The Co-Co interactions have positive values showing a ferromagnetic coupling between Co atoms. In the Co-Mn alloys, the Mn atoms are ferromagnetically coupled to the Co atoms and favor antiparallel coupling to the nearest Mn atoms, while the Co-Co interactions are ferromagnetic. All J_{ij}'s decay fast with distance. Increased Mn content is found to enhance all

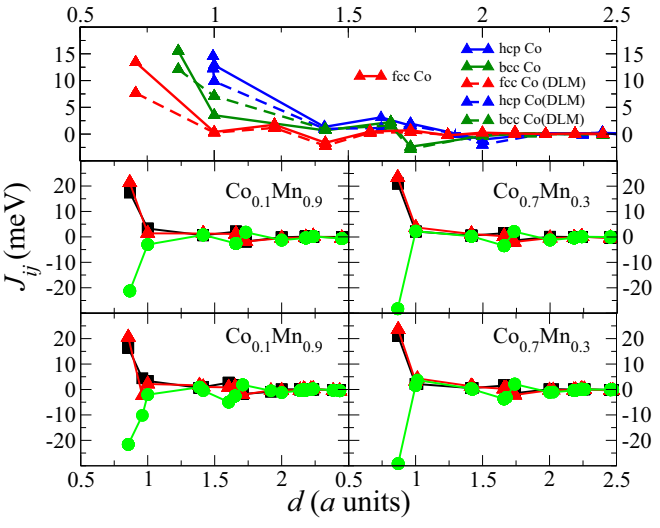

FIG. 4. Exchange integrals (J_{ij}) from FM configuration for fcc, hcp, and bcc Co (up triangle) are represented in solid lines, DLM (with dashed lines), and bcc and bct $Co_{1-x}Mn_x$ alloys plotted as a function of distance d (in a lattice parameter units). $J_{\text{Co-Co}}$ are labeled by filled red triangles, $J_{\text{Co-Mn}}$ by filled black squares, and $J_{\text{Mn-Mn}}$ by filled green circles. The exchange parameters are obtained for the FM state.

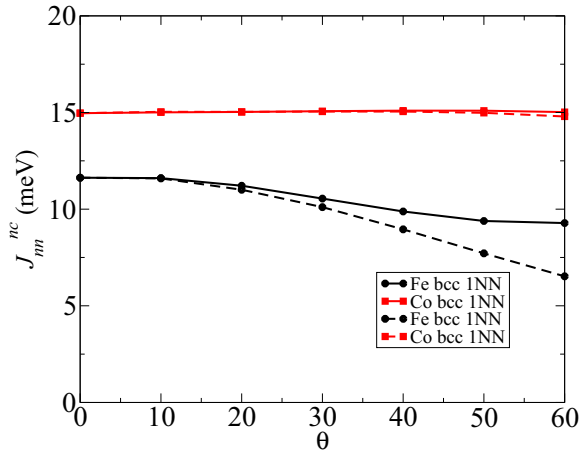

FIG. 5. Solid lines: noncollinear exchange coupling J_{ij}^{nc} defined by Eq. (5) for first-neighbor spin pairs in bcc Fe and Co when one spin is fixed and the spin directions at its first-neighbor sites are rotated by θ and ϕ. Dashed lines: noncollinear exchange coupling J_{ij}^{nc} defined by Eq. (5) for first-neighbor spin pairs in bcc Fe and Co when one spin is rotated by θ and ϕ. The azimuthal angle ϕ is set by a random number generator.

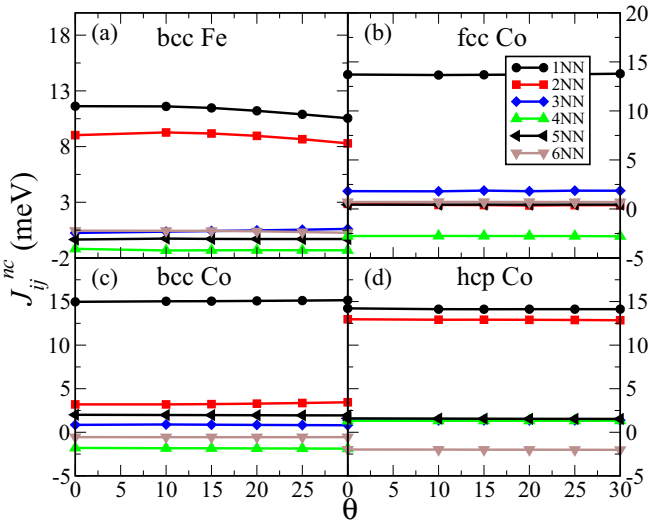

FIG. 6. Noncollinear exchange coupling J_{ij}^{nc} defined by Eq. (5) for the first six neighbor spin pairs in bcc Fe when one spin is fixed and the spin directions at its first-neighbor sites are rotated by θ and ϕ. Similar for the first six neighbor spin pairs in fcc, bcc, and hcp Co systems, respectively. In these figures, the azimuthal angle ϕ is set by a random number generator.

interactions, which can be explained by an increase of m_{Co} and m_{Mn} since, according to Eq. (1), the magnitude of the moments is effectively contained within the J_{ij}'s. The results obtained for the different phases of elemental Co are in overall good agreement with prior DFT studies, the differences coming from the employed computational methods [54–58].

To continue the analysis of exchange interactions in these systems, we investigated whether hcp, fcc, and bcc Co have Heisenberg exchange parameters that are configuration (temperature) dependent. To this end, we determined J_{ij}^{nc} defined by Eq. (5). Note that the second term in Eq. (4) did not give a significant contribution in Co systems we considered here. We compare these results to those of bcc Fe which has been already shown to have J_{ij}'s that are configuration dependent, and hence not to be a perfect Heisenberg system [59]. Note that $\vec{e}_i$ in Eq. (4) denotes the direction of the spin at site i, which can be formulated as $\vec{e}_i = \vec{e}(\theta_i, \phi_i)$, where θ_i and ϕ_i are the polar and azimuthal angles of the spin direction, respectively. The most simple noncollinear spin configuration may be the case when one spin in a ferromagnetic background is being rotated by a finite angle θ. The dashed lines in Fig. 5 show the J_{ij}^{nc}'s for the nearest-neighbor couplings in bcc Co and bcc Fe. We find that bcc Fe is more configuration dependent than bcc Co, i.e., bcc Co is closer to a "perfect" Heisenberg system. However, Fig. 2 shows that this story is somewhat more complex since for single-site rotation, the magnetic moment changes significantly with angle of rotation. As was already demonstrated for the case of spin spirals (Fig. 3), there is no contradiction since J_{ij} value is defined in such a way that it contains the magnetic moment value in itself. Thus, we witness once again that bcc Co reflects the physics intrinsic to an ideal Heisenberg magnet despite the sensitivity of its magnetic moment to the environment.

A more realistic spin configuration can be constructed when one spin is fixed at, say, site i, and where the spin directions at its first-neighbor sites are rotated by θ and ϕ. These results are shown by the solid lines in Fig. 5, modeling a finite-temperature disordered background. For such a configuration, we also calculated the J_{ij}^{nc}'s for neighbors, with varying distance. Figure 6 shows all the interatomic exchange coupling parameters for the first six nearest-neighbor shells in bcc Fe, fcc Co, bcc Co, and hcp Co, respectively. As can be seen, all the Co phases seem to have an excitation spectrum that is close to an ideal Heisenberg system, but again it is due to a decrease of the individual moments and an increase of the Heisenberg exchange interaction $\tilde{J}_{ij}$, as given by Eq. (2).

The findings presented above motivate that atomistic spin-dynamics simulations can be made from Heisenberg exchange parameters from collinear ferromagnetic phases of bcc, fcc, and hcp Co, if the definition of Eq. (1) is used for the energy excitations. As mentioned above, of all systems investigated here, elemental Co stands out to be unique in this regard.

The J_{ij}'s of Co-Mn alloys are evaluated only in the DLM phase (not shown) and only for alloy composition $x = 0.1$ and 0.3 since the aforementioned approach is cumbersome to apply for random alloys due to methodological reasons. The nearest-neighbor $J_{\text{Co-Co}}$, $J_{\text{Co-Mn}}$, and $J_{\text{Mn-Mn}}$ interactions are reduced compared to the value of the pure element by 21%, 26%, 7%, respectively, for $x = 0.1$ and 35%, 24%, 38%, respectively, for $x = 0.3$. These variations are in the same order as those obtained for Co in the DLM phase. Hence, Co and doped Co tend to behave like a "bad" Heisenberg system close to the phase transition temperature. In the low-temperature regime, however, exchange parameters of Mn are likely to change (not shown here), similar to Fe, giving evidence for a non-Heisenberg behavior of CoMn even at low temperature.

3. *Curie temperatures*

The calculated and experimental values of the Curie temperatures of Co-based systems are presented in Table I. The calculated Curie temperature values of bcc, fcc, and hcp

Co are in a rather good agreement with experimental data. The measured Curie temperatures of ferromagnetic $Co_{1-x}Mn_x$ alloys decrease linearly with an increase of concentration of Mn and become zero around 0.4. The calculated Curie temperature of $Co_{1-x}Mn_x$ alloys decrease linearly up to 30% of Mn and the T_C's are somewhat overestimated when compared with experimental values. We address this discrepancy to slight variations of the Heisenberg parameter with Mn doping at the phase transition temperature. This finding is supported by the reduced T_C values calculated in DLM configuration for $Co_{0.9}Mn_{0.1}$ and $Co_{0.7}Mn_{0.3}$ (see Table I). Since the difference in the phase transition temperature between the FM and the DLM phase is small compared to the maximal temperature obtained for the simulated pump-probe experiment, we make the approximation that a small amount of Mn in Co-Mn alloys will not change the temperature independence of the Heisenberg exchange parameters. Hence, the extracted FM collinear parameters are used in simulated pump-probe experiments of bcc, fcc, and Co, as well as bcc and bct Co-Mn alloys, as detailed below.

4. Damping parameters

Results for the Gilbert damping parameter of pure Co as well as for $Co_{1-x}Mn_x$ alloys calculated at $T = 324$ K are presented in Table I together with the DOS(E_F). In the case of pure bcc Co, this temperature corresponds approximately to the minimum of the $\alpha(T)$ curve, that indicates the crossover of the contributions due to the intraband (dominating at low temperature) and the interband (dominating at high temperature) electron scattering events [64]. In the case of $Co_{1-x}Mn_x$ alloys, on the other hand, the interband spin-flip scattering events are responsible for magnetization dissipation in the whole temperature regime, similar to the case of Cu impurities in Ni [26]. When the temperature increases above room temperature (not shown here), the thermal lattice vibrations lead for Co as well as $Co_{1-x}Mn_x$ alloys to an increase of $\alpha(T)$.

As can be seen in Table I, an increase of the Mn concentration x for bcc $Co_{1-x}Mn_x$ results in a decrease of the Gilbert damping, which correlates well with a decrease of the total DOS(E_F). For the atom-resolved damping parameters, we also find its correlation with the value of the DOS(E_F)/atom. With increasing Mn concentration in these alloys, the damping parameter of Mn spins and DOS(E_F)/atom both tend to increase, while the opposite is found for the Co spins. Comparing the Gilbert damping for the bcc and bct phases of $Co_{0.90}Mn_{0.10}$ ($Co_{0.70}Mn_{0.30}$), we find that the damping reaches higher values in bct phase than in bcc for both sublattices, which is in contrast to the DOS(E_F)/atom. This point also indicates that other effects also play a role in determining the damping parameter, and that the correlation between damping and DOS is strongest for alloys within the same crystal structure.

B. Dynamical properties

1. Dispersion relations

The calculated dynamical structure factor or magnon spectrum $S^z(\vec{q},\omega)$ of fcc, bcc, and hcp Co along the high-symmetry directions of the Brillouin zone are presented in Fig. 7. In these simulations, we used the exchange parameters reported in Fig. 4 and the Gilbert damping of 0.005. The fcc Co magnon dispersion along Γ-X high-symmetry path is in good agreement with experimental magnon data [65]. The hcp Co magnon dispersion along Γ-M and Γ-A high-symmetry path agrees also quite well with experimental magnon data already reported in Refs. [66,67]. Also, the results in Fig. 7 are consistent with results published by Etz *et al.* [68].

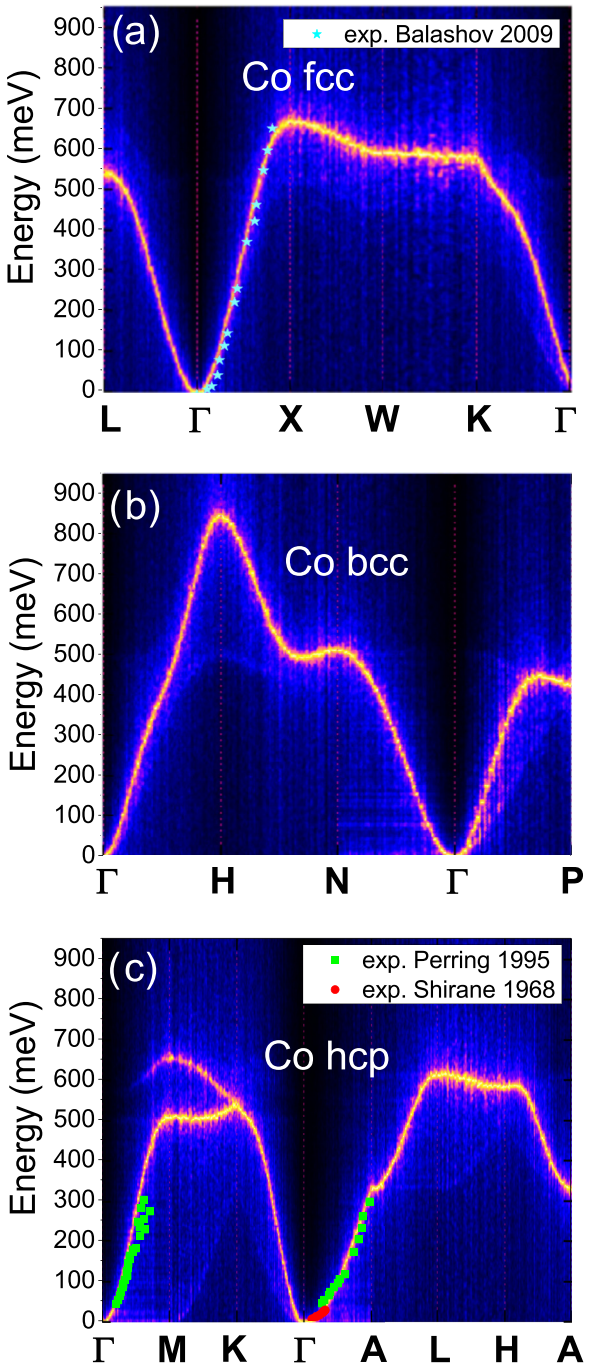

FIG. 7. Magnon dispersion relation of fcc, bcc, and hcp Co along high-symmetry directions of the Brillouin zone. Dots represent experimental measurements from Ref. [65]. All simulations were done assuming a negligibly low temperature and in FM state.

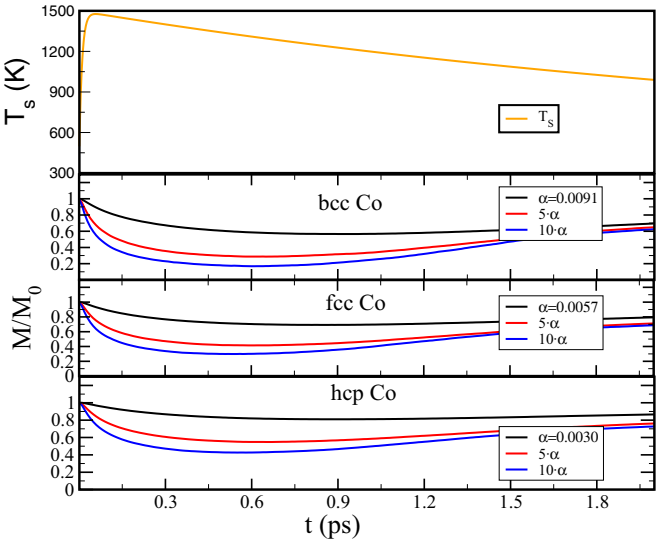

FIG. 8. Time-dependent normalized average magnetization (M/M_0) dynamics of Co systems after ultrashort laser irradiation (constant fluency) for different damping values with FM state. Top panel shows time-dependent spin temperature. The exchange parameters are obtained from SPR-KKR calculations. M_0 is magnetization at 300 K.

2. *Ultrafast magnetization under laser fluence*

In the following section, we present ultrafast magnetization dynamics of fcc, bcc, and hcp Co as well as bcc and bct Co-Mn alloys under the influence of a femtosecond laser pulse. The results are obtained by the integration of the atomistic LLG equation in combination with the analytical two-temperature model [69], and are plotted in Fig. 8. The simulated laser pulse results in a temperature profile that initially starts at room temperature as initial temperature T_0 and reaches its maximum at $T_P = 1500$ K and finally relaxes to $T_F = 450$ K via several scattering processes (see top panel of Fig. 8). The exponential parameters $\tau_{\text{initial}} = 1 \times 10^{-14}$ s and $\tau_{\text{final}} = 3 \times 10^{-12}$ s are used in the 2TM model. Damping values taken from the first-principles theory are considered in the simulations, called α, but also artificially enhanced values of the damping are used to investigate how the damping influences the ultrafast magnetization dynamics. The enhancement considered is 5 and 10 times larger, i.e., $5 \times \alpha$ and $10 \times \alpha$. The magnetization decreases rapidly to a minimum of about 44% to 84% of the total magnetization in fcc Co, 42% to 84% in bcc Co, and 20% to 57% in hcp Co for different damping values, as shown in Fig. 8.

As Fig. 8 shows, the quenching of magnetization increases with the increase of damping parameter. This highlights the fact that both the demagnetization time and the reduction

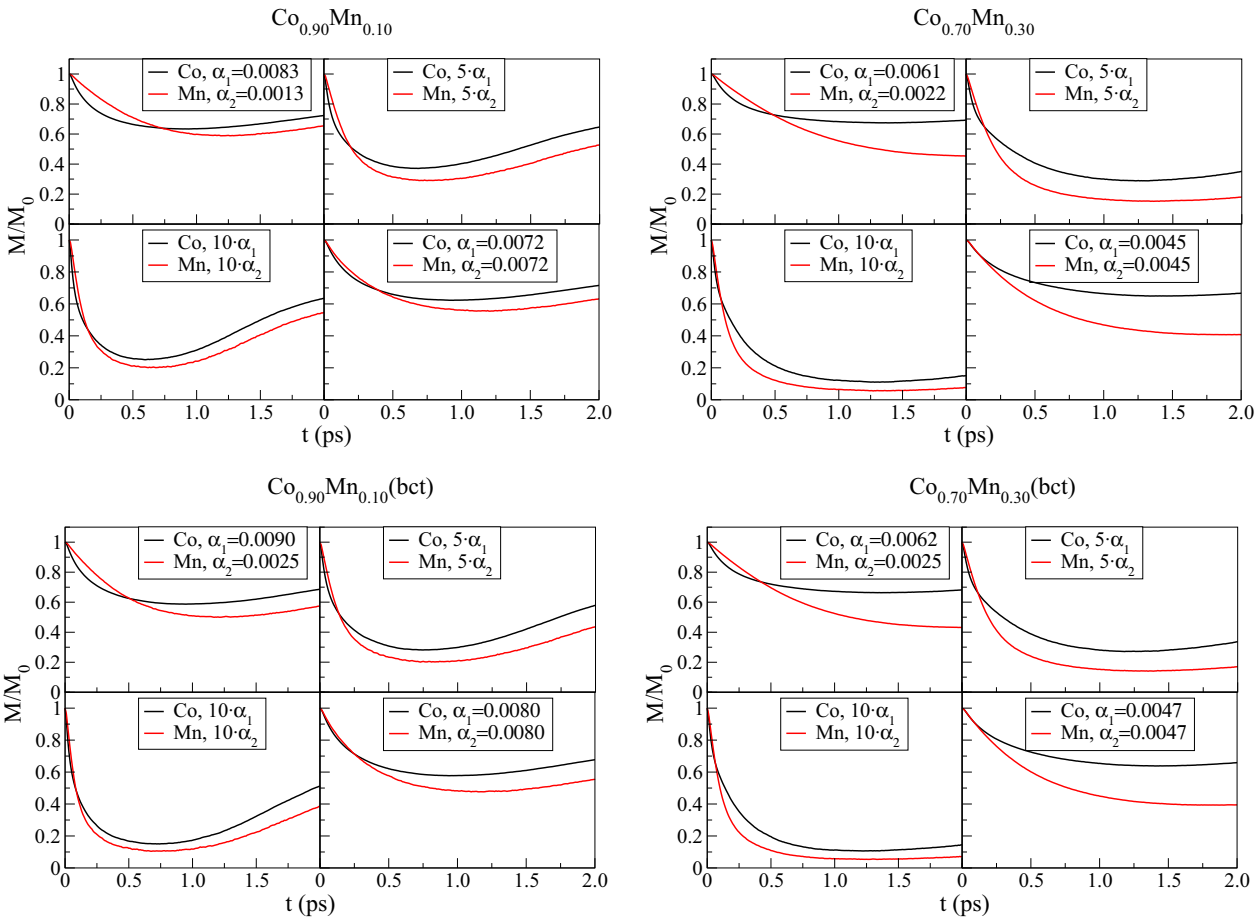

FIG. 9. Time evolution of the normalized average magnetization (M/M_0) of $Co_{0.90}Mn_{0.10}$ and $Co_{0.85}Mn_{0.15}$ and alloys under the influence of a thermal heat pulse for different sublattice damping parameters with FM state. The black and red lines represent the Co and Mn sublattices, respectively. The damping parameters α_1 and α_2 refer to Co and Mn sublattices, respectively. The exchange parameters are obtained from SPR-KKR calculations.

TABLE II. Element-specific demagnetization times for Co-based systems. α_1 refers to Co and α_2 refers to Mn. Experimental data from polycrystalline samples presented in brackets.

System	Co τ_{de} (ps)	Mn τ_{de} (ps)
fcc Co ($\alpha = 0.0057$)	0.255 [0.15–0.25] [11]	
bcc Co ($\alpha = 0.0091$)	0.250[0.15–0.25] [11]	
hcp Co ($\alpha = 0.0030$)	0.300[0.15–0.25] [11]	
$Co_{0.90}Mn_{0.10}$ ($\alpha_1 = 0.0083, \alpha_2 = 0.0013$)	0.219	0.6
$Co_{0.90}Mn_{0.10}$ ($\alpha = 0.0072$)	0.22	0.375
$Co_{0.70}Mn_{0.30}$ ($\alpha_1 = 0.0061, \alpha_2 = 0.0022$)	0.23	1.0
$Co_{0.70}Mn_{0.30}$ ($\alpha = 0.0045$)	0.5	0.65
$Co_{0.90}Mn_{0.10}$ bct ($\alpha_1 = 0.0090, \alpha_2 = 0.0025$)	0.215	0.56
$Co_{0.90}Mn_{0.10}$ bct ($\alpha = 0.0080$)	0.225	0.375
$Co_{0.70}Mn_{0.30}$ bct ($\alpha_1 = 0.0062, \alpha_2 = 0.0025$)	0.22	0.7
$Co_{0.70}Mn_{0.30}$ bct ($\alpha = 0.0047$)	0.45	0.6

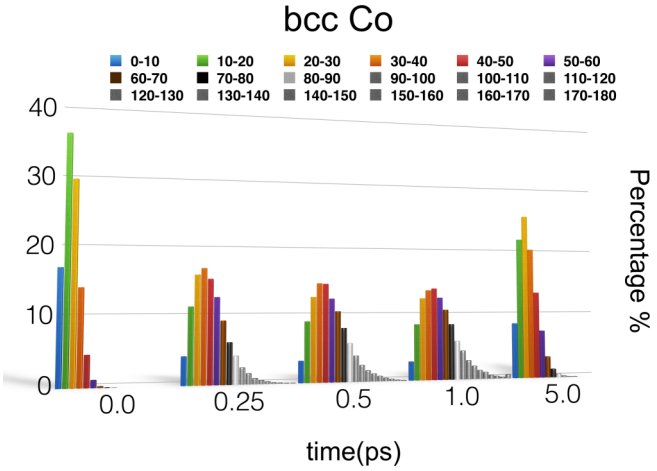

FIG. 10. The time evolution of the distribution of the azimuthal angle θ, for the different atomic spins for bcc Co. Note that the distribution is shown in intervals 0°–10°, 10°–20°, etc., where each interval is shown as a bar with a specific color. The distribution is shown for $t = 0$ ps, 0.25 ps, 0.5 s, 1.0 ps, and 5.0 ps after the laser pulse starts to heat up the sample.

of the magnetic moment in laser-induced demagnetization measurements depend critically upon the damping parameter. Furthermore, Fig. 9 shows that for systems with more than one magnetic sublattice, the magnetization dynamics may be different and that these sublattices therefore display different demagnetization times. The demagnetization times are calculated using a double exponential fitting function, as described in Ref. [70] and τ_m are listed in Table II. We would like to avoid a detailed comparison between the obtained theoretical and experimental demagnetization times because the theoretical values are calculated for single-crystal phases while the measurements are made for polycrystalline samples, potentially with several crystallographic phases present. However, the gross features of the numbers listed in Table II may be comparable to experimental data [11]. To end this section, in Table II, it is shown that the demagnetization time is reduced for increasing value of the damping parameter in agreement with the findings published in Refs. [71,72].

In Fig. 10 we show the distribution of azimuthal angles (θ) of the atomic spins during the demagnetization process, for bcc Co. Note that at each time, the distribution of the θ angles is found to follow essentially a Boltzmann distribution function. This is not an obvious result since the atomic spins are in out-of-equilibrium situation. We have also calculated the angles between the nearest-neighbor spins (not shown) and found that at each time step, these angles do not exceed 90°. As we have shown above (Fig. 3), the magnetic excitation energies in bcc Co are represented accurately in this interval of angles using Eq. (1) (see also Fig. 5), which lends credence to the approach adopted here to study ultrafast magnetization dynamics.

Next, we analyze the Co-Mn alloys in more detail, and we focus on $Co_{0.90}Mn_{0.10}$ and $Co_{0.70}Mn_{0.30}$ in the bcc and bct structures, respectively. Element-specific damping parameters [α_1 (Co), α_2 (Mn)] of Co-Mn alloys are used to investigate the angular momentum exchange between the sublattices in the spin-dynamics simulations. Results are presented in Fig. 9. The calculated element-specific demagnetization and remagnetization of Co-Mn alloys show a variety of possible situations that can be encountered in laser experiments on alloys with two magnetic sublattices. The demagnetization of Co precedes that of Mn by 0.15–0.6 ps due to the low damping value of Mn. The increase of damping parameters on both sublattices by 5 to 10 times in all considered alloys reduces the relative difference between the sublattice magnetism in the demagnetization phase. Furthermore, our results show that the quenching of magnetization on both sublattices increases with the increased damping parameter. For the lowest damping value of Mn in bcc $Co_{0.70}Mn_{0.30}$, the Mn demagnetization time is ∼4 times slower than that of the demagnetization of Co. The results of Fig. 9 show that a large asymmetry in the damping parameter in multicomponent magnets is a good parameter to use when one wants to identify systems with very different behavior of the demagnetization in ultrafast pump probe experiments. We propose that this is a parameter that should be explored when one tries to identify alloys and compounds in which the element-specific magnetization dynamics is drastically different. We hope these results can motivate further experimental studies.

V. CONCLUSION

With the extension of LKAG *ab initio* interatomic exchange calculation method for noncollinear spin systems, we have analyzed the exchange interactions and magnetic moments of Co in fcc, bcc, and hcp crystal structures. We found that elemental Co is unique in that it has excitations energies that reflect an almost perfect Heisenberg system in a rather wide range of angles between the spins. This has a significant importance in the correct description of the time evolution of the atomic magnetic moments under the influence of a temperature-dependent laser pulse. Note that in contrast to Co, bcc Fe shows significant spin configuration dependence, for any definition of the spin Hamiltonian, as it was shown here and in previous studies [17].

Mn spins, on the contrary, exhibit strongly non-Heisenberg behavior already for small degree of interatomic noncollinearity. A relatively small amount of Mn dopants, as in the case of the alloys studied here, is not expected to drastically alter the system's properties. We note, however, that high Mn concentration will definitely lead to the breakdown of the Heisenberg picture, and we plan to investigate it in detail in future.

The calculated structural and magnetic properties of Co-rich Co-Mn alloys are compared with experimental data. We find that they are in very good agreement with observations. The calculated T_C's reproduce well the measured values and show a linear decrease as a function of increasing Mn content, in line with the experiments. The magnon dispersion curves of fcc, bcc, and hcp Co are plotted along the high-symmetry directions of the Brillouin zone and they are indeed in good agreement with experimental data, where comparison can be made.

We have also addressed the temporal behavior of the magnetism of Co in the bcc, fcc, and hcp structures as well as Co-Mn alloys, after a laser excitation. Ultrafast magnetization dynamics of these Co systems was studied for different damping parameters, and it was found that the demagnetization behavior depends critically on the damping parameter as well as the strength of the exchange interaction represented by different concentrations of Mn. This becomes especially interesting for Co-Mn alloys that have very different values of the damping parameters and exchange interactions of the constituents, which lead to drastically different magnetization dynamics of the Co and Mn sublattices.

ACKNOWLEDGMENTS

The authors thank T. Silva, J. Shaw, M. Schoen, and A. N. Yaresko (MPI Stuttgart) for fruitful discussions. We acknowledge financial support from the Swedish Research Council. O.E. acknowledges financial support from KAW (Projects No. 2013.0020 and No. 2012.0031). O.E. and E.K.D.-Cz. acknowledge STandUP for financial support. The calculations were performed at NSC (Linköping University, Sweden) under a SNAC project.

[1] E. Beaurepaire, J. C. Merle, A. Daunois, and J. Y. Bigot, Phys. Rev. Lett. **76**, 4250 (1996).
[2] A. Kimel, A. Kirilyuk, A. Tsvetkov, R. Pisarev, and T. Rasing, Nature (London) **429**, 850 (2004).
[3] A. V. Kimel, B. A. Ivanov, R. V. Pisarev, P. A. Usachev, A. Kirilyuk, and T. Rasing, Nat. Phys. **5**, 727 (2009).
[4] J. Y. Bigot, L. Guidoni, E. Beaurepaire, and P. N. Saeta, Phys. Rev. Lett. **93**, 077401 (2004).
[5] I. Tudosa, C. Stamm, A. B Kashuba, F. King, H. C. Siegmann, J. Stohr, G. Ju, B. Lu, and D. Weller, Nature (London) **428**, 831 (2004).
[6] J. Y. Bigot, M. Vomir, and E. Beaurepaire, Nat. Phys. **5**, 515 (2009).
[7] K. Vahaplar, A. M. Kalashnikova, A. V. Kimel, S. Gerlach, D. Hinzke, U. Nowak, R. Chantrell, A. Tsukamoto, A. Itoh, A. Kirilyuk, and T. Rasing, Phys. Rev. B **85**, 104402 (2012).
[8] C. Stamm, T. Kachel, N. Pontius, R. Mitzner, T. Quast, K. Holldack, S. Khan, C. Lupulescu, E. F. Aziz, M. Wietstruk, H. A. Dürr, and W. Eberhardt, Nat. Mater. **6**, 740 (2007).
[9] H. S. Rhie, H. A. Dürr, and W. Eberhardt, Phys. Rev. Lett. **90**, 247201 (2003).
[10] B. Koopmans, H. Kicken, M. van Kampen, and W. de. Jonge, J. Magn. Magn. Mater. **286**, 271 (2005).
[11] B. Koopmans, G. Malinowski, F. Dalla Longa, D. Steiauf, M. Fähnle, T. Roth, M. Cinchetti, and M. Aeschlimann, Nat. Mater. **9**, 259 (2010).
[12] O. Eriksson, A. Bergman, L. Bergqvist, and J. Hellsvik, *Atomistic Spin Dynamics: Foundations and Applications* (Oxford University Press, Oxford, UK, 2017).
[13] R. Chimata, A. Bergman, L. Bergqvist, B. Sanyal, and O. Eriksson, Phys. Rev. Lett. **109**, 157201 (2012).
[14] V. P. Antropov, M. I. Katsnelson, B. N. Harmon, M. van Schilfgaarde, and D. Kusnezov, Phys. Rev. B **54**, 1019 (1996).
[15] A. I. Liechtenstein, M. I. Katsnelson, V. P. Antropov, and V. A. Gubanov, J. Magn. Magn. Mater. **67**, 65 (1987).
[16] R. F. L. Evans, U. Atxitia, and R. W. Chantrell, Phys. Rev. B **91**, 144425 (2015).
[17] A. Szilva, M. Costa, A. Bergman, L. Szunyogh, L. Nordström, and O. Eriksson, Phys. Rev. Lett. **111**, 127204 (2013).
[18] The Munich SPR-KKR package, version 6.3, H. Ebert *et al.*, http://ebert.cup.uni-muenchen.de/SPRKKR; H. Ebert, D. Ködderitzsch, and J. Minár, Rep. Prog. Phys. **74**, 096501 (2011).
[19] O. K. Andersen, Phys. Rev. B **12**, 3060 (1975).
[20] P. R. Peduto, S. Frota-Pessoa, and M. S. Methfessel, Phys. Rev. B **44**, 13283 (1991).
[21] V. Antonov, B. Harmon, and A. Yaresko, *Electronic Structure and Magneto-Optical Properties of Solids* (Kluwer, Dordrecht, 2004).
[22] P. Weinberger and R. Podloucky, Phys. Rev. B **22**, 645 (1980); J. Staunton, B. L. Györffy, and P. Weinberger, J. Phys. F: Met. Phys. **10**, 2665 (1980).
[23] P. Soven, Phys. Rev. **156**, 809 (1967).
[24] A. J. Pindor, J. Staunton, G. M. Stocks, and H. Winter, J. Phys. F: Met. Phys. **13**, 979 (1983).
[25] J. Staunton, B. Györffy, A. Pindor, G. Stocks, and H. Winter, J. Magn. Magn. Mater. **45**, 15 (1984).
[26] H. Ebert, S. Mankovsky, D. Ködderitzsch, and P. J. Kelly, Phys. Rev. Lett. **107**, 066603 (2011).
[27] D. Böttcher, A. Ernst, and J. Henk, J. Magn. Magn. Mater. **324**, 610 (2012).
[28] P. Lloyd, Proc. Phys. **90**, 207 (1967).
[29] H. Ebert and S. Mankovsky, Phys. Rev. B **79**, 045209 (2009).
[30] https://openlibrary.org/works/OL3517103W/Relativistic_electron_theory.
[31] W. H. Butler, Phys. Rev. B **31**, 3260 (1985).
[32] S. Mankovsky, D. Ködderitzsch, G. Woltersdorf, and H. Ebert, Phys. Rev. B **87**, 014430 (2013).
[33] U. Bovensiepen, J. Phys.: Condens. Matter **19**, 083201 (2007).
[34] K. Binder, Z. Phys. B **43**, 119 (1981); Phys. Rev. Lett. **47**, 693 (1981).

[35] J. P. Perdew, K. Burke, and M. Ernzerhof, Phys. Rev. Lett. **77**, 3865 (1996).
[36] V. L. Moruzzi, J. F. Janak, and K. Schwarz, Phys. Rev. B **37**, 790 (1988).
[37] B. Skubic, J. Hellsvik, L. Nordström, and O. Eriksson, J. Phys.: Condens. Matter **20**, 315203 (2008).
[38] Y. U. Idzerda, W. T. Elam, B. T. Jonker, and G. A. Prinz, Phys. Rev. Lett. **62**, 2480 (1989).
[39] G. R. Harp, R. F. C. Farrow, D. Weller, T. A. Rabedeau, and R. F. Marks, Phys. Rev. B **48**, 17538 (1993).
[40] G. Y. Guo and H. H. Wang, Chin. J. Phys. **38**, 949 (2000).
[41] G. S. Dong, Y. Z. Wu, C. Jing, Y. Chen, W. R. Zhu, X. F. Jin, H. W. Zhao, M. Lu, H. R. Zhai, X. L. Shen, and L. Li, J. Cryst. Growth **187**, 444 (1998).
[42] D. Wu, G. L. Liu, C. Jing, Y. Z. Wu, D. Loison, G. S. Dong, X. F. Jin, and D.-S. Wang, Phys. Rev. B **63**, 214403 (2001).
[43] L. Zhang, D. Basiaga, J. R. O'Brien, and D. J. Heiman, J. Appl. Phys. **98**, 106101 (2005).
[44] H. W. Zhao, Y. Chen, W. R. Zhu, G. S. Dong, X. F. Jin, M. Lu, and H. R. Zhai, J. Appl. Phys. **81**, 2036 (1997).
[45] G. A. Prinz, Phys. Rev. Lett. **54**, 1051 (1985).
[46] A. Díaz-Ortiz, R. Drautz, M. Fähnle, H. Dosch, and J. M. Sanchez, Phys. Rev. B **73**, 224208 (2006).
[47] *American Institute of Physics Handbook* (3rd ed.), edited by B. H. Billins and D. E. Gray (McGraw-Hill, New York, 1972).
[48] J. A. C. Bland, R. D. Bateson, P. C. Reidi, R. G. C. Graham, H. J. Lauter, J. Penfold, and C. Shackleton, J. Appl. Phys. **69**, 4989 (1991).
[49] O. Eriksson, B. Johansson, R. C. Albers, A. M. Boring, and M. S. S. Brooks, Phys. Rev. B **42**, 2707 (1990).
[50] X. Liu, M. M. Steiner, R. Sooryakumar, G. A. Prinz, R. F. C. Farrow, and G. Harp, Phys. Rev. B **53**, 12166 (1996).
[51] http://materials.springer.com/bp/docs/978-3-540-39667-3.
[52] L. M. Sandratskii, J. Phys.: Condens. Matter **3**, 8565 (1991).
[53] S. V. Halilov, H. Eschrig, A. Y. Perlov, and P. M. Oppeneer, Phys. Rev. B **58**, 293 (1998).
[54] M. van Schilfgaarde and V. P. Antropov, J. Appl. Phys. **85**, 4827 (1999).
[55] M. Pajda, J. Kudrnovský, I. Turek, V. Drchal, and P. Bruno, Phys. Rev. B **64**, 174402 (2001).
[56] I. Turek, J. Kudrnovský, V. Drchal, P. Bruno, and S. Blügel, Phys. Status Solidi B **236**, 318 (2003).
[57] M. Lezaić, P. Mavropoulos, and S. Blügel, Appl. Phys. Lett. **90**, 082504 (2007).
[58] Y. O. Kvashnin, W. Sun, I. Di Marco, and O. Eriksson, Phys. Rev. B **92**, 134422 (2015).
[59] Y. O. Kvashnin, R. Cardias, A. Szilva, I. Di Marco, M. I. Katsnelson, A. I. Lichtenstein, L. Nordström, A. B. Klautau, and O. Eriksson, Phys. Rev. Lett. **116**, 217202 (2016).
[60] J. Crangle, Philos. Mag. **46**, 499 (1955).
[61] A. Vega and W. Nolting, Phys. Status Solidi B **193**, 177 (1996).
[62] C. M. Singal and T. P. Das, Phys. Rev. B **16**, 5068 (1977).
[63] M. Acet, C. John, and E. F. Wassermann, J. Appl. Phys. **70**, 6556 (1991).
[64] K. Gilmore, Y. U. Idzerda, and M. D. Stiles, Phys. Rev. Lett. **99**, 027204 (2007).
[65] P. Buczek, A. Ernst, and L. M. Sandratskii, Phys. Rev. B **84**, 174418 (2011); T. Balashov, Ph.D. thesis, Physikalisches Institut, Universität Karlsruhe (TH), 2009.
[66] G. Shirane, V. J. Minkiewicz, and R. Nathans, J. Appl. Phys. **39**, 383 (1968).
[67] T. Perring, A. Taylor, and G. Squires, Phys. B (Amsterdam) **213-214**, 348 (1995).
[68] C. Etz, L. Bergqvist, A. Bergman, A. Taroni, and O. Eriksson, J. Phys.: Condens. Matter **27**, 243202 (2015).
[69] R. Chimata, L. Isaeva, K. Kadas, A. Bergman, B. Sanyal, J. H. Mentink, M. I. Katsnelson, T. Rasing, A. Kirilyuk, A. Kimel, O. Eriksson, and M. Pereiro, Phys. Rev. B **92**, 094411 (2015).
[70] S. Mathias, C. La-O-Vorakiat, P. Grychtol, P. Granitzka, E. Turgut, J. M. Shaw, R. Adam, H. T. Nembach, M. E. Siemens, S. Eich, C. M. Schneider, T. J. Silva, M. Aeschlimann, M. M. Murnane, and H. C. Kapteyn, Proc. Natl. Acad. Sci. USA **109**, 4792 (2012).
[71] C. L. S. Kantner, M. C. Langner, W. Siemons, J. L. Blok, G. Koster, A. J. H. M. Rijnders, R. Ramesh, and J. Orenstein, Phys. Rev. B **83**, 134432 (2011).
[72] B. Koopmans, J. J. M. Ruigrok, F. DallaLonga, and W. J. M. de Jonge, Phys. Rev. Lett. **95**, 267207 (2005).